Airborne Wind Lidar Measurements of Vertical and Horizontal Winds for the Investigation of Orographically Induced Gravity Waves

BENJAMIN WITSCHAS, STEPHAN RAHM, ANDREAS DÖRNBRACK, JOHANNES WAGNER, AND MARKUS RAPP

Institut für Physik der Atmosphäre, Deutsches Zentrum für Luft- und Raumfahrt (DLR), Oberpfaffenhofen, Germany

(Manuscript received 23 January 2017, in final form 11 April 2017)

ABSTRACT

Airborne coherent Doppler wind lidar measurements, acquired during the Gravity Wave Life-Cycle (GW-LCYCLE) I field campaign performed from 2 to 14 December 2013 in Kiruna, Sweden, are used to investigate internal gravity waves (GWs) induced by flow across the Scandinavian Mountains. Vertical wind speed is derived from lidar measurements with a mean bias of less than 0.05 m s^{-1} and a standard deviation of 0.2 m s^{-1} by correcting horizontal wind projections onto the line-of-sight direction by means of ECMWF wind data. The horizontal wind speed and direction are retrieved from lidar measurements by applying a velocity–azimuth display scan and a spectral accumulation technique, leading to a horizontal resolution of about 9 km along the flight track and a vertical resolution of 100 m, respectively. Both vertical and horizontal wind measurements are valuable for characterizing GW properties as demonstrated by means of a flight performed on 13 December 2013 acquired during weather conditions favorable for orographic GW excitation. Wavelet power spectra of the vertical wind speed indicate that the horizontal GW wavelengths lay mainly between 10 and 30 km and that the GW amplitude above the mountain ridge decreases with increasing altitude. Additionally, the perturbations of the horizontal wind speed are analyzed, showing horizontal wavelengths in the excitation region of 100–125 km with upwind-tilted wave fronts. By means of elevation power spectra, it is revealed that vertical wind power spectra are dominated by the short-wave elevation part, whereas horizontal wind perturbations are dominated by the long-wave part.

1. Introduction

Internal waves are waves that oscillate within a stratified fluid. If the fluid is considered to be the atmosphere and the restoring force of vertical displaced air parcels is provided by buoyancy, such waves are called internal gravity waves or just gravity waves (GWs). GWs are ubiquitous in the atmosphere and their impact on the vertical transport and exchange of energy and momentum between the troposphere and the middle atmosphere is well known (Fritts and Alexander 2003). GWs are commonly excited in the troposphere by flow over orography (e.g., Smith et al. 2008; Teixeira 2014), convection (e.g., Vadas et al. 2012), or flow deformation, for instance, caused by jets and fronts (Plougonven and Zhang 2014). Although there is a general understanding of processes launching GWs, the nature of wave source spectra is more complex and less well understood. For example, steady flow over topographic features will launch GWs of zero ground phase velocity (Smith 1989). However, the spectrum generated by unsteady flow over complex topography and the associated nonlocal effects are much less well understood (Chen et al. 2007). Thus, a better characterization of GW sources is still an outstanding issue needed for a proper description of the dynamical coupling of the lower and middle atmosphere.

To study the entire life cycle of GWs starting from their generation at low altitudes over their propagation and finally dissipation, the Gravity Wave Life-Cycle (GW-LCYCLE) I field campaign was conducted from 2 to 14 December 2013 in northern Scandinavia (Wagner et al. 2017; Ehard et al. 2016). As it has been shown in the past, the region above the Scandinavian Mountains is well suited for studies of coupling between the troposphere and the middle atmosphere (Dörnbrack et al. 2001), and the region is promising because of the north–south orientation of the Scandinavian mountain ridge and the accompanying mountain wave generation induced

Corresponding author: Benjamin Witschas, benjamin.witschas@dlr.de

DOI: 10.1175/JTECH-D-17-0021.1

by westerly blowing winds. Besides a variety of ground-based instruments, the German Aerospace Center [Deutsches Zentrum für Luft- und Raumfahrt (DLR)] deployed the Falcon research aircraft, equipped with a coherent Doppler wind lidar (DWL) measuring horizontal and vertical wind speeds. A detailed summary of the GW-LCYCLE I campaign, including an overview of airborne observations, numerical simulations, and a discussion of the synoptic situation during the campaign period, has recently been provided by Wagner et al. (2017) and Ehard et al. (2016). In this study, the DWL measurements performed during GW-LCYCLE I are discussed in detail and shown to be a valuable tool for GW source spectra characterization.

Lidar instruments in general allow for deriving various atmospheric parameters range resolved and thus enable investigating GW characteristics in several altitudes simultaneously. Usually, the temperature perturbations derived from ground-based Rayleigh lidar or resonance-lidar data are used for that purpose (Baumgarten 2010; Hildebrand et al. 2012). For instance, Kaifler et al. (2015) used temperature perturbations derived from Rayleigh lidar measurements (28–76 km altitude) to characterize GWs over New Zealand and showed that enhanced GW potential energy densities in the mesosphere are surprisingly associated with mountain waves excited by only low to moderate tropospheric wind speeds between 2 and 12 m s^{-1}.

Although the aforementioned lidar technique represents a valuable tool to characterize GWs, it is mostly limited to nighttime operation and altitudes above 20 km. Thus, no information about the excitation region at lower altitudes can be derived, which is needed to distinguish different excitation sources (e.g., flow over orography, convection, flow deformation) and to study GW propagation involving processes such as secondary wave generation in the tropopause region or reflection/secondary wave generation in the lower stratosphere (Smith et al. 2008). Moreover, ground-based lidar measurements cannot be used to study the spatial evolution and distribution of GWs. An airborne DWL system, however, yields line-of-sight (LOS) wind speed measurements per 1 s, and hence with a horizontal and vertical resolution of a few hundred meters, making it a promising instrument for accurate GW characterization in the troposphere.

The usefulness of airborne vertical wind measurements was, for instance, demonstrated by Whiteway et al. (2003) and Duck and Whiteway (2005), who studied spectra of GWs, turbulence, and GW breaking at the tropopause region by means of in situ data acquired on different flight levels. Compared to such kinds of in situ measurements, horizontal and vertical winds can be measured by lidar at several altitudes simultaneously. Bluman and Hart (1988) used airborne Doppler wind measurements (from 3 km to the ground) to validate linear lee-wave model calculations, Weissmann et al. (2005a) investigated the vertical transport from the boundary layer into the free troposphere, and Kiemle et al. (2007) made use of airborne DWL data in combination with water vapor measurements of a differential absorption lidar in order to estimate the latent heat flux in the boundary layer. Recently, Chouza et al. (2016) showed that vertical wind speed can be retrieved from airborne DWL measurements with a mean systematic uncertainty of 0.05 m s^{-1} and that the data are valuable for characterizing island-induced GWs. They also revealed that adequate corrections of horizontal wind projections onto the LOS direction have to be done in order to retrieve reliable vertical wind speeds from airborne DWL measurement data.

In this paper, the setup, the measurement procedures, and corresponding data retrieval and correction methods of DLR's airborne coherent DWL are discussed. Although the DWL has been in operation since 1999, no detailed description of the optical layout and the retrieval procedures has been published so far. For the first time, ECMWF horizontal wind data are used to correct LOS wind speeds in order to retrieve vertical wind with a mean bias of less than 0.05 m s^{-1} and a horizontal resolution (along flight track) of 200 m. Furthermore, horizontal wind speeds are retrieved from DWL measurements by means of a modified spectral accumulation technique. Based on these data, horizontal wind speed perturbations are calculated and are shown to be valuable for GW characterization. The usefulness of DWL data for GW characterization is revealed by means of measurements acquired from a flight on 13 December 2013 performed during a mountain wave event in the framework of the GW-LCYCLE I campaign. The paper is structured as follows: In section 2, a detailed description of the airborne coherent DWL is given, followed by an explanation of the data retrieval and correction methods for vertical and horizontal wind speeds (section 3). In section 4, both horizontal and vertical wind lidar data are used to characterize GWs concerning their spectral features and propagation behavior.

2. Instrument description

Over the years, DLR's coherent DWL system has been successfully deployed in several ground-based and airborne field campaigns targeting various objectives, such as measuring aircraft wake vortices (Köpp et al. 2004), aerosol optical properties (Chouza et al. 2015), and horizontal wind speeds over the Atlantic Ocean as input data for assimilation experiments (Weissmann

et al. 2005b). A general overview of DWL applications for atmospheric research and an overview of previous airborne campaigns with DLR's coherent DWL are given by Reitebuch (2012). Recently, the system was used in the framework of three airborne field campaigns aiming to characterize the life cycle of GWs namely during the GW-LCYCLE I campaign (Wagner et al. 2017; Witschas et al. 2016), the Deep Propagating Gravity Wave Experiment (DEEPWAVE) campaign (Fritts et al. 2016; Smith et al. 2016), and the GW-LCYCLE II campaign.

To characterize orographically induced GWs—so-called mountain waves—both horizontal and vertical wind measurements with high horizontal and vertical resolution and a low statistical uncertainty are desired. All of these goals are met with the DWL. Horizontal and vertical winds are retrieved by either applying the velocity–azimuth display (VAD) technique (Browning and Wexler 1968) or steering the beam to nadir direction, leading to a horizontal resolution of about 9 or 0.2 km, respectively. The vertical resolution of 100 m for both measurement modes is determined by the laser pulse length.

A schematic block diagram of the DWL system is shown in Fig. 1. The transceiver was developed and built by CLR Photonics (today Lockheed Martin Coherent Technologies) (Henderson et al. 1991, 1993; Hannon and Henderson 1995); the double-wedge scanner system and the data acquisition unit were developed at DLR.

The transceiver unit comprises a single-frequency continuous-wave master oscillator (MO) that is used as an injection seeder for the slave oscillator (SO) and additionally used as a local oscillator for the coherent heterodyne detection. The MO is a diode-pumped Tm:LuAG laser characterized by a low bandwidth providing high heterodyne efficiency. A part of the MO radiation is coupled into the SO under a small angle of about 1° via an acousto-optic modulator (AOM) that additionally acts as a Q-switch. When the AOM is switched on, the MO is aligned to match the optical axis of the SO and thus enables adequate seeding. Further, the MO frequency is shifted by 100 MHz, permitting determination of the magnitude and sign of the frequency difference between MO and SO, which is later needed for wind measurements. The SO is based on a two-side pumped Tm:LuAG crystal and produces laser pulses with a wavelength of 2022.54 nm (vacuum), a pulse energy of 1–2 mJ, and a pulse length of 400 ns (≈ 120 m) at a pulse repetition rate of 500 Hz, leading to an average transmitted laser power of 0.5–1.0 W. The laser wavelength of 2022.54 nm allows for an eye-safe operation in an atmospheric window with low absorption of water vapor, enabling wind measurements up to a range of 12 km.

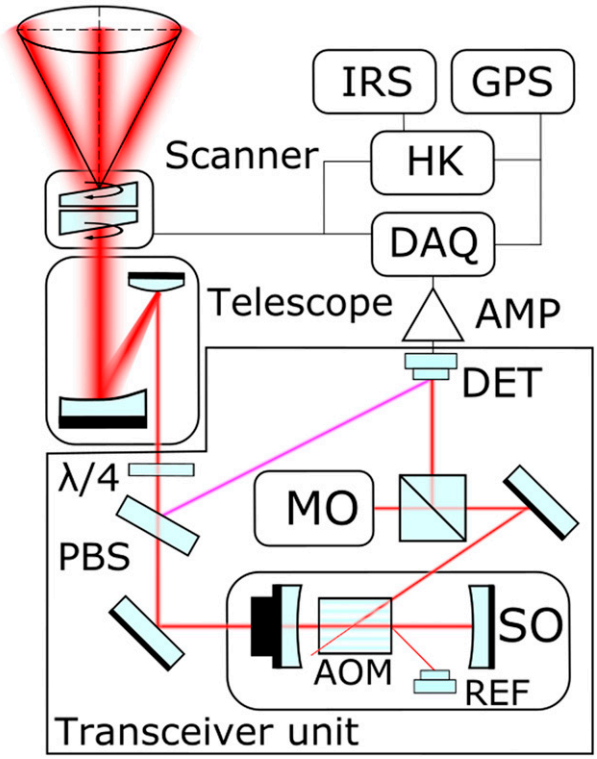

FIG. 1. Simplified sketch of DLR's coherent DWL system (not to scale) indicating the transceiver unit, including local oscillator (MO), slave oscillator (SO), acousto-optical modulator (AOM), reference pulse detector (REF), polarizing beam splitter (PBS), and detector (DET). Additionally, the acquisition chain, including signal amplifier (AMP), data acquisition unit (DAQ), housekeeping data acquisition unit (HK), global positioning system (GPS), inertial reference system (IRS) and the beam-expanding telescope and the double-wedge scanner, is shown.

Furthermore, the pulse repetition rate of 500 Hz provides the possibility of signal accumulation, which reduces speckle noise. In addition, the laser beam has a nearly Gaussian shape in the spatial, temporal, and spectral domain, which reduces the uncertainty of the Doppler estimates. To ensure resonance between the SO cavity length and the MO radiation, the SO cavity length is controlled by the ramp and fire technique (Henderson et al. 1986), where the resonance signal is monitored by the reference detector (REF).

After the SO, the laser beam is passing a polarizing beam splitter (PBS) that is used to separate the outgoing laser pulse and the signal backscattered from the atmosphere, and to protect the sensitive detector form the emitting laser pulse. Before the laser beam is expanded to a diameter of about 10 cm by means of a telescope, its polarization is changed to circular by means of a quarter-wave plate (λ/4). The expanded laser beam then enters an optical double-wedge scanner that enables

steering the laser beam to any position within a cone angle of 30°. The scanner itself is composed of two antireflection-coated rotating silicon wedges, especially doped to be transparent for the 2022.54-nm wavelength. The wedge angle is 6.0° and the index of refraction is 3.452 (at 2022.54 nm). The actual wedge positions for the desired beam direction are set by two stepper motors working with a microstepping driver that is controlled by the housekeeping computer (HK).

Once traveling through the atmosphere, a small portion of the emitted laser pulse partly scatters on aerosols and cloud particles back to the lidar system, where it is received with the same telescope that was used for emission. The backscattered light is reflected on the PBS and directed to the optical signal detector (DET), where it is mixed with a portion of the MO laser. After preamplification directly at the detector, the analog detector signal is additionally amplified by a custom-made 500-MHz amplifier (AMP). In particular, the internal reference pulse is attenuated by 9 dB and the atmospheric signal is amplified by 24 dB such that they reach a comparable signal level before digitization. Now, the time-resolved detector signal resulting from each single-laser shot is sampled with 500 MHz and 8-bit resolution (Agilent U1064A, Acqiris DC241) before it is stored to a solid-state drive connected to a dedicated computer (ADLINK, ePCIS-6400x) (DAQ). This procedure leads to a data rate of about 15 MB s^{-1} and gives maximum flexibility for postprocessing.

To achieve a high timing accuracy for the data processing, all measured quantities (time-resolved laser pulse signal, scanner position, aircraft position, speed, and attitude angles) are stored with an accurate time stamp generated by a custom-made global positioning system (GPS)-controlled oscillator. In particular, a 10-MHz signal of an oven-controlled crystal oscillator is fed into a timer/counter module (National Instruments, Ni-PXI-6608). Here, the signal is divided by 100 in order to reach a 100-kHz clock signal that is synchronized by the pulse-per-second signal provided by the GPS module (Septentrio, PolaRx2), which is additionally used to measure the aircraft position and speed with a temporal resolution of 1 Hz. The latter one is important, as the aircraft speed ($\approx$200 m s^{-1}) is the main contributor to the measured Doppler shift (i.e., larger than the expected horizontal wind speed) and thus has to be considered in order to retrieve the actual wind speed reliably. The 100-kHz time stamp is also sent to the DAQ computer, where it is acquired (NI PXI-6602) and stored together with each single-laser pulse.

In addition to the aircraft speed, the aircraft attitude has to be measured and considered for wind retrieval. For that reason, roll, pitch, and yaw angles are measured with an inertial reference system (IRS; Honeywell LASEREF YG 1779) whose data, including time stamp, are also stored on the HK computer. The velocity and the actual position of the aircraft are obtained by GPS. The accuracy of the horizontal velocity measured with the GPS receiver is specified to be 1.5 mm s^{-1} (1σ level). The main parameters of the DWL are summarized in Table 1.

TABLE 1. Overview of the DWL system parameters.

Laser	
Laser active medium	Tm:LuAG
Wavelength (vacuum; nm)	2022.54
Repetition rate (Hz)	500
Energy/pulse (mJ)	1–2
Output power (W)	0.5–1
Pulse length (FWHM)[a]	$\approx$400 ns ($\approx$120 m)
Frequency offset (MHz)	100 ± 2
Transceiver	
Telescope type	Off axis
Telescope diameter (m)	0.11
Scanner	
Type	Double wedge
Wedge angle (°)	6.0
Maximum displacement (°)	30
Detector	
Type	InGaAs PIN photodiode
Data acquisition	
Type	Single shot
Sample frequency (MHz)	500
Resolution (bit)	8

[a] FWHM denotes the full width at half maximum.

3. Measurement procedure and wind retrieval

To measure vertical profiles of either the three-dimensional wind vector or the vertical wind speed, the DWL was operated in two different modes: namely, scanning mode and fixed LOS mode. While operating in scanning mode, a conical step-and-stare scan (a VAD technique) around the vertical axes with a nadir angle of 20° is performed. A total of 24 LOS wind velocities are measured per one scanner revolution and are used to retrieve the three-dimensional wind vector as described in section 3c. Considering a 1-s averaging time for each LOS measurement (24 s), 21 s for the scanner motion between each measurement position, and an aircraft speed of about 200 m s^{-1}, the spatial resolution of horizontal wind data is about 9 km. Operating in fixed LOS mode, the laser beam is intentionally pointed to nadir direction and thus the measured LOS wind equals the vertical wind speed. Considering a 1-s averaging time, the horizontal resolution for the retrieved vertical wind profiles is about 200 m. As it is difficult to sustain an

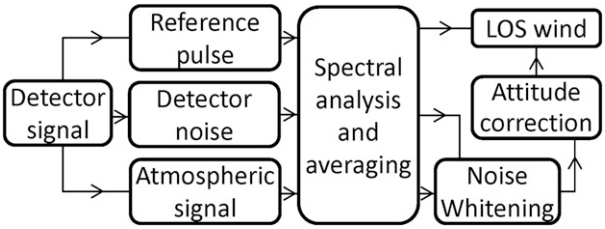

FIG. 2. Schematic overview of the LOS wind processing procedure.

exact nadir pointing due to the permanent aircraft movement around the attitude angles (pitch, yaw, and roll), projections of the horizontal wind speed contaminate the vertical wind measurements and need to be corrected.

a. LOS wind

The basis for both the horizontal and vertical wind retrieval are LOS winds that are retrieved from the detector raw signal, which itself is stored for each single-laser pulse with a sampling rate of 500 MHz, an 8-bit resolution, and a duration of $t = 97.8\,\mu$s. This leads to an overall sampling range of $r = ct/2 = 14.659$ km, which is sufficient, as the distance to ground is always lower considering a maximum flight altitude of 12 km and maximum off-nadir angles of 30°. A schematic overview of the LOS wind processing steps is given in Fig. 2.

The single-shot data storage enables excluding bad pulses and correcting the laser frequency variations from pulse to pulse before accumulation (e.g., all valid laser pulses within 1 s). To do so, the power spectrum of the reference pulse signal, which is the beat signal of the local oscillator (MO) and the emitted laser pulse, is calculated and analyzed regarding its frequency. If the beat frequency differs by more than 10% of the nominal AOM frequency of 100 MHz, or if the laser pulse build-up time is larger than 3.5 μs (default value is 2.3 μs), then the laser pulse is not considered for accumulation. Moreover, before accumulating the respective reference pulse spectra, they are frequency shifted to a defined reference value of, for example, 100 MHz in order to correct for pulse-to-pulse frequency variations and thus to avoid spectral broadening in the accumulation process. The applied frequency shift is afterward equally applied to the atmospheric signal power spectra. The part of the detector raw signal containing the atmospheric return is divided into segments that lead to 100-m range gates in the vertical by considering the actual laser beam pointing angle, the aircraft altitude and attitude, and the reference pulse timing. After that, the power spectrum is calculated for each range gate and laser pulse, is frequency shifted according to the reference pulse frequency shift and, subsequently, accumulated. The detector signal at the end of the record is used to analyze the detector noise characteristics, which is especially important in the weak signal regime (Frehlich et al. 1997; Beyon et al. 2012). As the system is operated from an aircraft, the signal after the ground return can certainly be considered to contain just noise. As the shot noise signal level induced by the local oscillator is about 12 dB higher than the one of other noise sources, the system can be considered to be shot-noise limited. The power spectrum of the noise signal is calculated for each single laser pulse and is additionally averaged over 1 s or rather 500 pulses. Consequently, each power spectrum for each single range gate is divided by the respective noise spectrum in order to correct for the system noise and the receiver frequency response (Fig. 2, noise whitening). Alternatively, the noise spectrum could be subtracted from the lidar raw signal. However, as shown by Frehlich et al. (1997), the spectral estimates would not be constant with frequency in that case. In the next step, the resulting power spectra are corrected for the actual LOS direction, which is derived as explicitly described by Chouza et al. (2016), and for the aircraft speed projected onto the LOS direction, which is derived from the ground speed measured by the GPS module and the actual laser beams' pointing direction.

The remaining frequency shift Δf between the reference pulse and the atmospheric signal is proportional to the wind speed v according to $\Delta f = (2f_0 v)/c$, where f_0 is the laser frequency, c is the velocity of light, and $\lambda_0 = c/f_0 = 2022.54$ nm is the laser wavelength. Using this relation, the actual LOS v is calculated.

To get the actual vertical wind speed, or rather the three-dimensional wind vector from respective LOS wind measurements, further processing steps are needed, as discussed below.

b. Vertical wind retrieval

Basically, the derived LOS wind speed equals the vertical wind speed in case the laser beam is pointing downward exactly in the nadir direction. Since 2014, the DWL system is equipped with an automatic flight attitude correction loop that keeps the set laser beams' pointing direction based on the aircraft IRS data. As such a correction loop was not available during the GW-LCYCLE I campaign in 2013, slight off-nadir angles of up to 1° occur during measurement due to a change in the aircraft attitude (Witschas et al. 2016). As a consequence, the LOS wind speed additionally contains a projection of the horizontal wind speed onto the LOS direction that has to be corrected. For instance, considering a horizontal wind speed of 30 m s^{-1} and an off-nadir angle of 0.5° toward the wind blowing direction, the LOS-projection is 0.26 m s^{-1}. As vertical

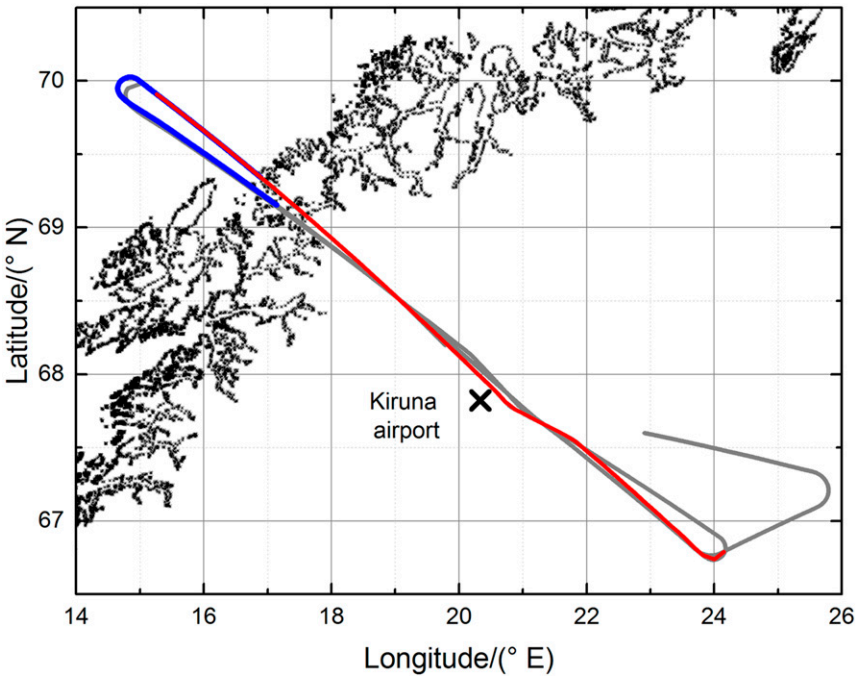

FIG. 3. Flight track of the research flight performed on 13 Dec 2013 (gray line). Location of Kiruna airport (black cross) and the flight segment used to demonstrate the vertical wind speed retrieval (dark blue line) are shown. Flight segment with wind vector measurements is indicated (red line).

wind speeds are expected to be small (e.g., a few meters per second during strong mountain wave events), the aforementioned effect has to be considered for a reliable vertical wind speed retrieval.

In principle, the actual LOS direction $\mathbf{n}_{\mathrm{los}}$ (with $|\mathbf{n}_{\mathrm{los}}| = 1$) and the actual horizontal wind vector $\mathbf{v}_{\mathrm{hor}}$ have to be known in order to calculate the projection of the wind vector onto the LOS direction v_{los} according to

$$v_{\mathrm{los}} = \mathbf{v}_{\mathrm{hor}} \cdot \mathbf{n}_{\mathrm{los}}, \tag{1}$$

where $\mathbf{n}_{\mathrm{los}}$ is calculated for each measurement by considering the position of both the scanner wedges and the lidar installation position, which is determined by exploiting information from the ground return signal (Chouza et al. 2016). The scanner incremental encoders provide a resolution of 144 000 per revolution (360°). Thus, the actual pointing position is known with an angular resolution of 0.0025°. Vector $\mathbf{v}_{\mathrm{hor}}$ can be principally provided by the lidar itself. Though, when the lidar is operating in fixed LOS mode, no information about the wind vector is available from measurements. For that reason, usually two or more legs are flown along the same mountain transect, giving both the wind vector and the vertical wind speed with a slight temporal difference of about 1 h. However, as the data coverage of both measurements can be different, not every LOS wind measurement may correspond to a wind vector measurement that can be used for correction.

Thus, to be able to correct all LOS measurements, the horizontal wind from European Centre for Medium-Range Weather Forecasts (ECMWF; T1279 L137, cycle 40r1) operational analyses on 137 model levels with a horizontal resolution of 16 km and a temporal resolution of 6 h, interpolated to the respective flight track and time, are used to calculate the LOS projection of the horizontal wind according to Eq. (1).

The functionality of this correction procedure is demonstrated based on the lidar measurements acquired on 13 December 2013, which are later used for GW characterization (section 4). The corresponding flight track is shown in Fig. 3 (gray line). The red line indicates a flight leg performed in scanning mode; the rest of the flight was measured with a fixed LOS (nadir pointing). The dark blue line indicates a flight segment of 1300 s (22 min) before and after a turn used to demonstrate the correction procedure. Assuming constant wind conditions and a zero mean vertical wind speed on this 133-km-long flight segment (one way), the measured vertical wind speeds at all altitudes are expected to follow a Gaussian distribution with zero mean. As shown in Fig. 4, the histograms of the uncorrected LOS winds before (orange) and after the

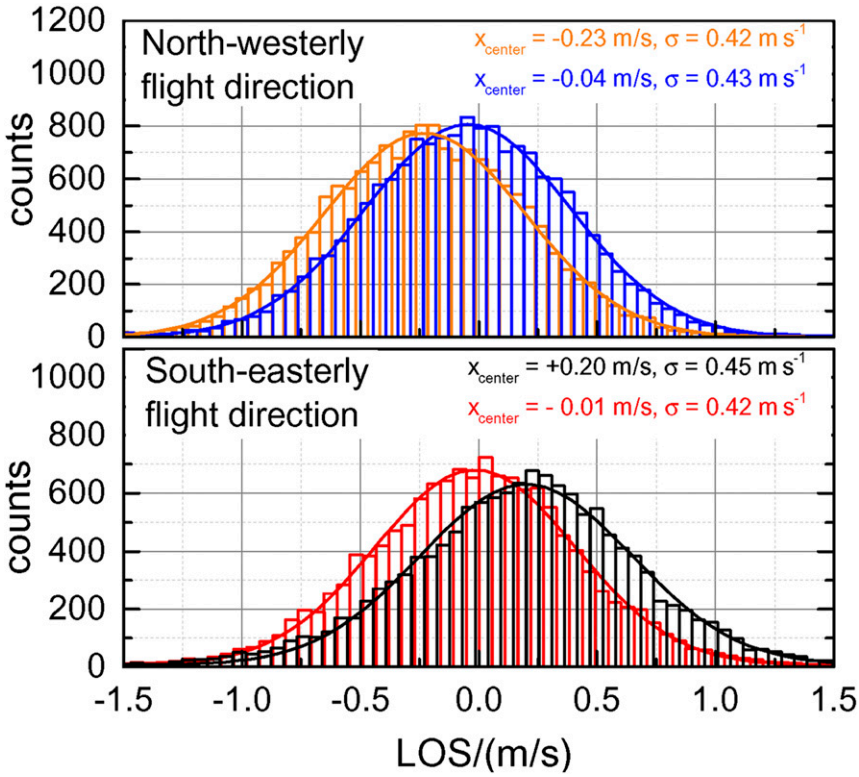

FIG. 4. Histogram of LOS wind speeds (13 Dec 2013) acquired while flying in (top) a northwesterly direction and (bottom) a southeasterly direction. Histograms of the uncorrected winds (orange and black) and that of the corrected winds (blue and red) are indicated; inset shows the respective mean value and standard deviation (same colors).

turn (black) indeed follow a Gaussian distribution with a standard deviation of 0.42 and 0.45 m s^{-1}, respectively, where both the Gaussian distribution and the nearly equal standard deviation confirm steady atmospheric conditions during the measurement. The mean values, however, are not zero but −0.23 and 0.20 m s^{-1}, respectively. Although the similar magnitude of the mean values again verifies stable atmospheric conditions during the measurement, the nonzero mean and the opposite sign clearly indicate that the LOS wind contains a projection of the horizontal wind and is not just containing vertical wind. The analysis of the actual laser pointing $\mathbf{n}_{\mathrm{los}}$ additionally confirms that the beam was pointing off nadir by about +1° before and −1° after the turn (not shown), leading to the observed offset. It is worth mentioning that the horizontal wind direction during that flight was about 315° (Fig. 10, bottom left) and thus the aircraft was flying with headwind while flying in a northwesterly direction and with tailwind while flying in a southeasterly direction.

Before ECMWF data are used for correction, horizontal wind speeds resulting from the lidar measurements performed in scanning mode (Fig. 3, red line) are used for model validation as indicated by Fig. 5, which shows ECMWF versus DWL data. From the scatterplot it can be seen that both datasets are in accordance. A line fit (Fig. 5, red dashed line) yields a correlation coefficient of $r^2 = 0.85$, a slope of 1.00, and an intercept of 0.01 m s^{-1} and thus demonstrates that ECMWF winds describe the measured horizontal wind speeds accurately. Assuming that the same accuracy is reached for the other flight legs, this comparison further illustrates that ECMWF wind speeds can be reliably used for the LOS wind correction. The overall standard deviation of $\sigma = 2.21$ m s^{-1} is most likely a result of the different horizontal resolutions of the model (16 km) and the lidar (9 km), and the representative error of lidar wind speeds caused by the inhomogeneous sampling during the VAD scan (Frehlich 2001a).

After correction the LOS winds yield the histograms shown in Fig. 4, for northwesterly flight direction (blue) and for southeasterly flight direction (red). They still follow a Gaussian distribution but the mean value is close to zero now. In particular, the remaining offsets are −0.04 and 0.01 m s^{-1}, respectively, while the standard deviation remains similar compared to the histograms, resulting

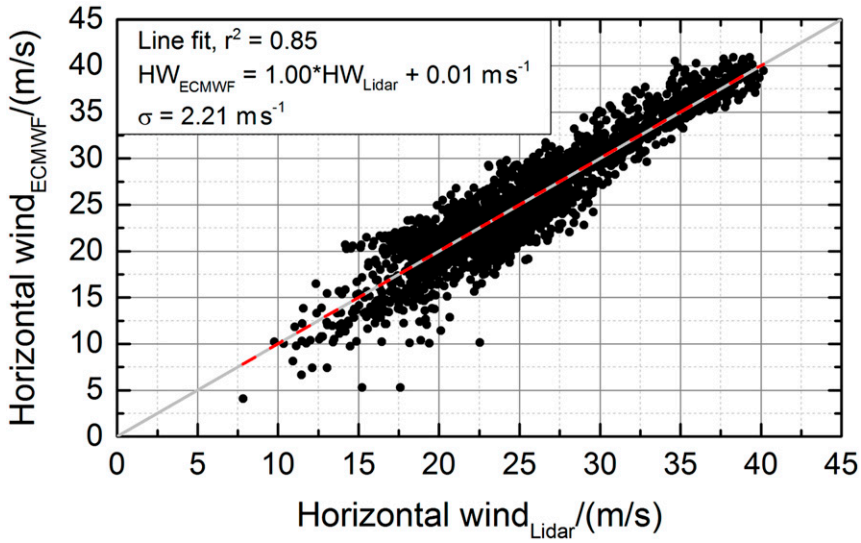

FIG. 5. ECMWF horizontal wind speeds vs lidar-measured wind speeds: $y = x$ line (gray line) and line fit to the dataset (red dashed line). Fit results are given by the inset; σ denotes the standard deviation of the data with respect to the line fit.

from the uncorrected data. This confirms the recently published results by Chouza et al. (2016), who estimated the mean systematic uncertainty of vertical wind speeds to be smaller than $0.05\,\mathrm{m\,s^{-1}}$ after correction.

To further estimate the statistical uncertainty of the vertical wind speed, the corresponding power spectrum (Fig. 6) is analyzed. As explicitly discussed by Frehlich (2001b) and O'Connor et al. (2010), the average of the constant high-frequency region of the power spectrum of the measured wind speed (Fig. 6, dashed vertical red line) gives an estimate of the random error produced by the average of the spectral estimates. By setting the cutoff frequency to $0.2\,\mathrm{Hz}$ ($\lambda \approx 1\,\mathrm{km}$), the resulting standard deviation is calculated to be $0.2\,\mathrm{m\,s^{-1}}$. It is

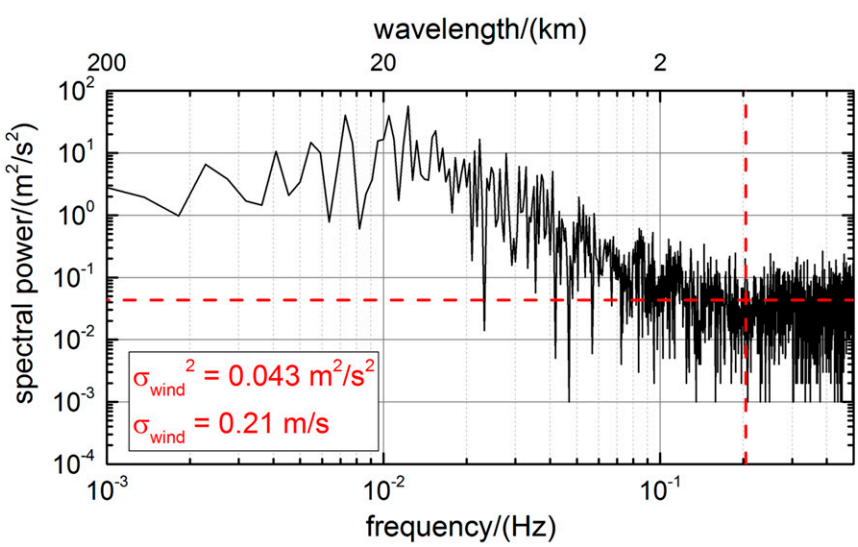

FIG. 6. Spectral power of vertical wind speed measured on 13 Dec 2013: cutoff frequency (0.2 Hz; vertical dashed red line), which is set and used for error estimation, and mean value of the noise level (horizontal dashed red line), which is considered to be the variance of the wind measurements (Frehlich 2001b). Estimated wind error is indicated in the insert. The wavelength λ (top x axis) is calculated by assuming a constant aircraft velocity of $v_{ac} = 200\,\mathrm{m\,s^{-1}}$ according to $\lambda = v_{ac}/f$.

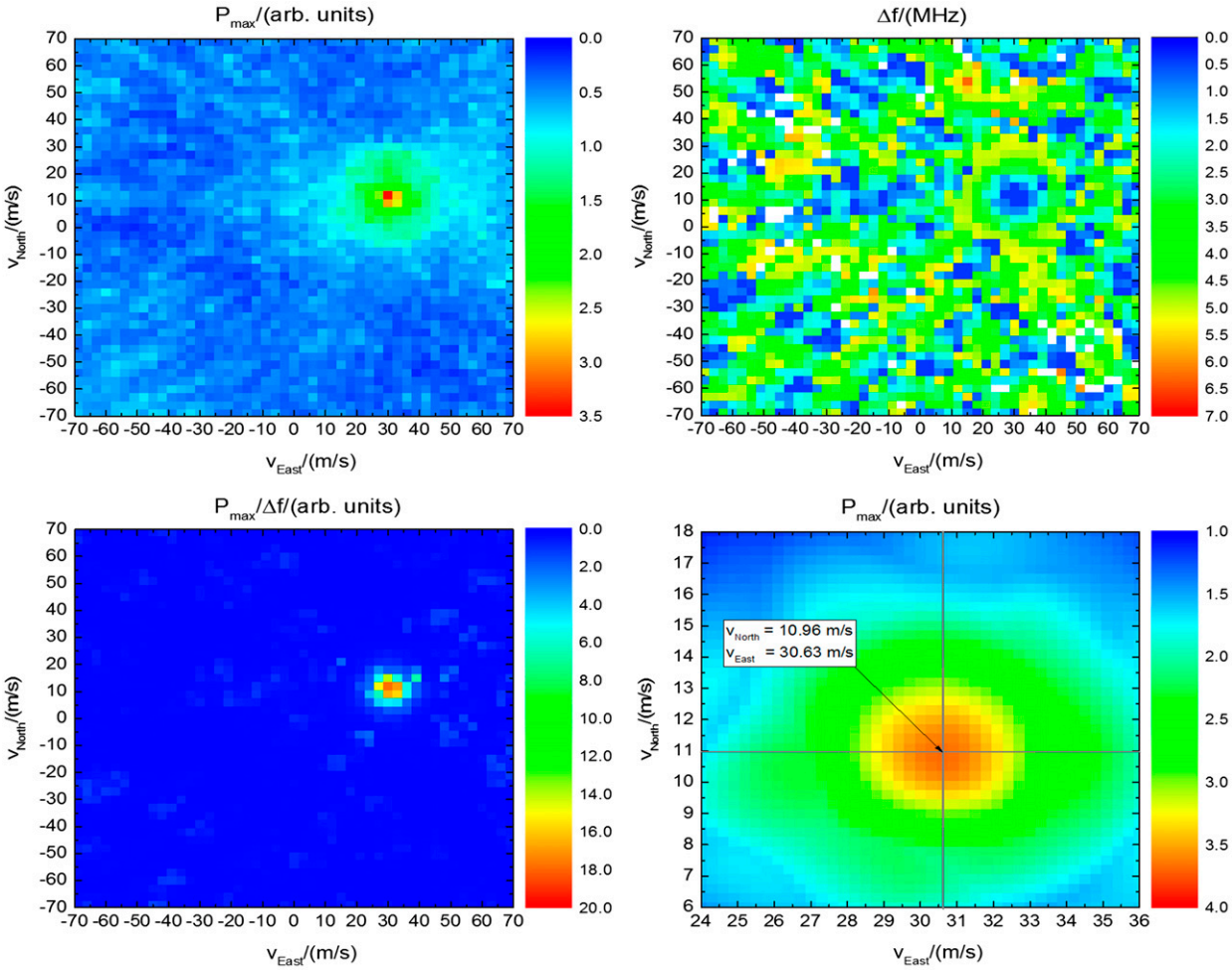

FIG. 7. Schematic illustration of wind vector estimation. (top left) Maximum value P_{max} of the accumulated power spectra for various hypothetical north and east wind components. (top right) Corresponding frequency deviations Δf of the peak maximum from zero frequency. (bottom left) Equation $P_{max}/\Delta f$ used for wind vector estimates. (bottom right) As in the bottom-left panel, but analyzed for a smaller velocity space ($\pm 6\,\mathrm{m\,s^{-1}}$ around the maximum value) with higher resolution ($0.3\,\mathrm{m\,s^{-1}}$).

worth mentioning that the same value is obtained if the cutoff frequency is set to 0.3 Hz ($\lambda \approx 0.7$ km), demonstrating insensitivity to this arbitrarily set quantity. Here, the wavelength λ is calculated by assuming a constant aircraft velocity of $v_{ac} = 200\,\mathrm{m\,s^{-1}}$ according to $\lambda = v_{ac}/f$, with f being the frequency.

c. *Horizontal wind and direction*

To measure the horizontal wind speed and direction with the DWL, a conical step-and-stare scan of the laser beam around the vertical axes with an off-nadir angle of 20° is performed with 24 LOS measurements per one scanner revolution of 360°. Various LOS, or rather radial velocities at different azimuth angles, are derived and analyzed, leading to the mean wind vector in the measurement volume. As summarized by Smalikho (2003), there are several techniques of wind vector estimation from DWL data. One method that leads to reliable wind vector estimates even at low signal-to-noise ratio (SNR) conditions is based on the maximum function of accumulated spectra (MFAS), which retrieves the wind vector without estimating single-radial wind velocities, as is necessary, for instance, when applying sine-wave fitting methods. A modified version of the MFAS algorithm that additionally exploits the frequency deviation of accumulated spectra from their nominal value to further increase the number of reliable wind vector estimates is first used in this study. The principle of the algorithm is schematically illustrated by Fig. 7.

First, all spectra of the 24 scan positions are shifted to be proportional to their azimuth angle and an assumed wind vector, where the north component v_{North} and the east component v_{East} are usually varied from −72 to

$+72\,\mathrm{m\,s^{-1}}$ with a step size of $3\,\mathrm{m\,s^{-1}}$ to cover all possible wind speeds with an adequate resolution. Afterward, all spectra are accumulated and the maximum of the accumulated spectrum $P_{\max}$ at frequency f_c is determined, leading to a 2D plot as shown in Fig. 7 (top left). In case the wind components match the real wind, the useful signal containing the wind information is accumulated, whereas the random noise signal level is decreased by $\sqrt{N_{\mathrm{VAD}}}$, where $N_{\mathrm{VAD}} = 24$ is the number of measurements per one scanner revolution. Thus, $P_{\max}$ is an estimate of the most likely wind vector.

By additionally analyzing the center frequency of the f_c, or rather the deviation from the expected frequency value f_0 with $\Delta f = |f_c - f_0|$ (Fig. 7, top right), it turned out that the contrast of the ratio $P_{\max}/\Delta f$ is remarkably better than the one of $P_{\max}$ alone (Fig. 7, bottom left) and thus leads to better wind vector estimates, or rather to a more reliable estimation of the actual $P_{\max}$ related to the wind speed. This is especially true in the case of having a low SNR. As Δf is an indirect measure of the mean vertical wind velocity, dividing $P_{\max}$ by Δf weights values closer to zero vertical wind velocity. To prevent division by zero or very small values, all values of $\Delta f < 0.2\,\mathrm{MHz}$ are set to $0.2\,\mathrm{MHz}$. In the future it is foreseen to measure the vertical wind component after three to four LOS measurements with a respective off-nadir angle in order to consider the actual vertical wind speed for the MFAS algorithm. This may further improve the retrieval procedure and may make the usage of $P_{\max}/\Delta f$ irrelevant.

In the last step, the same procedure is repeated for a smaller wind velocity space (usually $\pm 6\,\mathrm{m\,s^{-1}}$ around the maximum value) with a smaller step size (usually $0.3\,\mathrm{m\,s^{-1}}$) in order to further increase the accuracy (Fig. 7, bottom right). For this last step, just $P_{\max}$ is used for the wind retrieval in order to avoid any biases induced by dividing with Δf. Thus, the division with Δf is just performed to find the correct maximum of $P_{\max}$ reliably even at low SNR values. The wind itself is then retrieved in a smaller interval around this maximum without weighting. The maximum value of $P_{\max}$, or rather its center of gravity, is considered as the best estimate for the horizontal wind vector. For the example shown in Fig. 7 (bottom right), the retrieved wind vector is composed of $v_{\mathrm{North}} = 10.96\,\mathrm{m\,s^{-1}}$ and $v_{\mathrm{East}} = 30.63\,\mathrm{m\,s^{-1}}$.

4. Experimental results

The usefulness of airborne coherent DWL data for GW characterization is demonstrated by means of a research flight performed during the period 0600–0935 UTC 13 December 2013 (flight track shown in Fig. 3) during favorable conditions for mountain wave generation and vertical propagation. During the flight, lower-tropospheric winds were blowing with northwesterly directions (see Fig. 10) crossing the Scandinavian mountain ridge almost perpendicularly and thus providing excellent conditions for GW excitation. Furthermore, a strong and quasi-stationary tropopause jet impacted the vertical propagation of GWs into the stratosphere (Wagner et al. 2017).

Altogether, three legs were flown at three different altitudes and with different lidar acquisition modes. In particular, vertical wind measurements were performed during the first flight leg (0648–0725 UTC, flight altitude = 5.7 km, leg length = 495.5 km, horizontal resolution = 225 m; Fig. 8) and horizontal wind measurements were performed during the second flight leg (0731–0820 UTC, flight altitude = 7.4 km, leg length = 479.6 km, horizontal resolution = 7.74 km; Fig. 10). The third leg (no measurements shown) was flown with varying altitudes in order to provide different probing heights for the in situ instruments and is not further discussed. The main details of the two flight legs discussed in the following sections are summarized in Table 2.

a. Vertical wind measurements

The vertical wind derived from DWL measurements (section 3b) acquired during the first flight leg is shown in Fig. 8 (top). The vertical wind measured at flight level (5.7 km) by the nose-boom-mounted five-hole probe is additionally indicated by the bar at 5.7 km altitude. In Fig. 8 (bottom), the vertical wind measured by the lidar in an altitude of 4.9 km and the in situ–measured wind speed at flight level (5.7 km) are additionally displayed for comparison.

From Fig. 8 (top) it can be seen that the lidar data are acquired with almost full vertical coverage, except for the westernmost part of the flight leg, where low-level clouds prevented measurements down to the ground (white areas). The vertical wind speed westward of the mountains is measured to be close to $0\,\mathrm{m\,s^{-1}}$, as is expected for an undisturbed atmosphere. Above the mountain ridge however, pronounced GW structures with vertical wind speeds up to -3 and $4\,\mathrm{m\,s^{-1}}$ are observed ($\approx 19°-19.5°$E; distance = 250 km). The range-resolved lidar measurements further enable determining the GW wave fronts to be vertically orientated without any remarkable phase tilt from ground up to 5.7-km altitude. Looking at Fig. 8 (bottom) it can be seen that the vertical wind structure at 4.9 km measured by the lidar and at 5.7 km measured by the aircraft have the same characteristics and that the amplitude is decreasing slightly with increasing altitude.

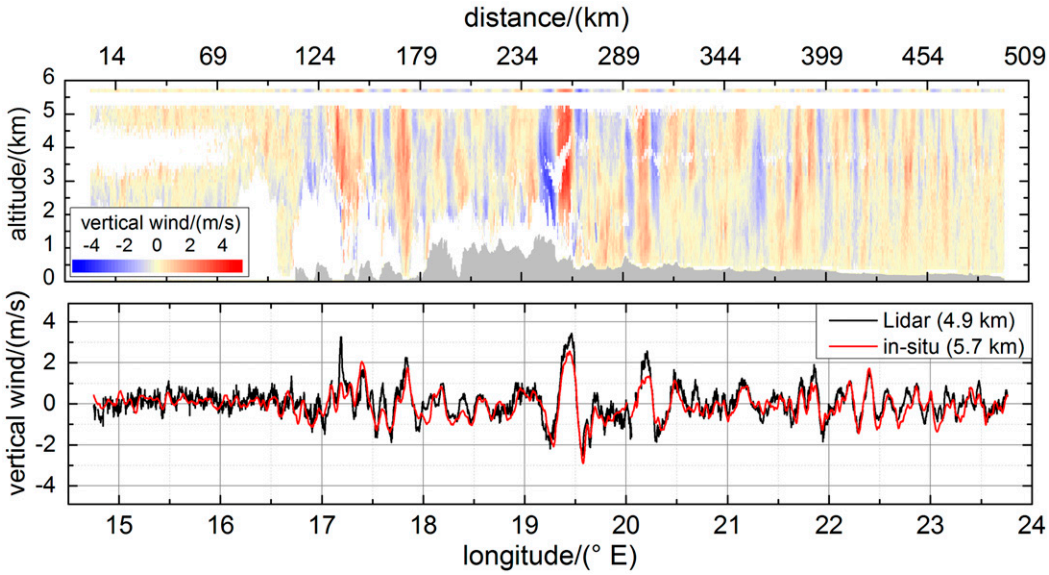

FIG. 8. (top) Cross section of vertical wind derived from lidar measurements (see section 3b) during a cross-mountain leg flown 0648–0725 UTC Dec 13 (flight altitude is 5.7 km, leg length is 495.5 km, horizontal resolution is 225 m). Bar at 5.7 km altitude indicates the in situ–measured vertical wind speed. Corresponding flight track is shown in Fig. 3. (bottom) Vertical wind derived from lidar measurements at 4.9 km (black) and in situ–measured vertical wind at 5.7 km (red).

To study the GW characteristics in more detail, wavelet power spectra of the vertical wind speed measured at different altitudes are calculated. The wavelet analysis is performed using a Morlet wavelet with a nondimensional frequency of $\omega_0 = 6$ and the power spectra are normalized such that they represent the squared amplitude of the vertical wind speed with a potential sinusoidal variation (Torrence and Compo 1998). To deal with the few data gaps in the vertical wind speed measurement, the wavelet analysis is performed for vertical wind speed averaged over 500 m, where each data point is the mean of at least two data points. If there are fewer than two data points available within the 500-m interval, then no mean vertical wind is calculated. The vertically averaged wind speeds (500 m) measured by the lidar (3.0–3.5, 4.0–4.5, 5.0–5.5 km), the in situ vertical wind measured by the aircraft (5.7 km), the elevation along the flight leg, and the corresponding wavelet power spectra are shown in Fig. 9.

From both the wind measurements and the wavelet power spectra it can be seen that the GWs with the largest amplitudes are excited in the region of the highest elevation (≈19°−19.5°E; distance = 250 km). The dominant horizontal wavelengths lay between 10 and 30 km and the amplitude of the GWs is continuously decreasing with increasing altitude. For instance, the amplitude of the distinct GW feature between ≈19° and 19.5°E is decreasing from $\pm 4\,\mathrm{m\,s^{-1}}$ (3–3.5 km) to $\pm 2\,\mathrm{m\,s^{-1}}$ at 5.7 km. Only at the eastern part of the flight leg (≈22.0°−22.5°E; distance = 420 km − 440 km) is there a GW feature showing an increasing amplitude with altitude.

The wavelet power spectrum of the elevation along the flight track (Fig. 9, bottom) shows two distinct regions: a short-wave region with wavelengths between 10 and 40 km, and a long-wave region with wavelengths between 80 and 150 km. The short-wave part of the spectrum is similar to the one of the vertical wind speed but slightly shifted to the location where the orography shows a pronounced structure at the respective wavelengths. The long-wave part of the elevation spectrum (80–150 km) is not represented in the vertical wind, meaning that short-wave orography modulations have a larger impact on the vertical wind speed spectrum.

TABLE 2. Overview of flight legs performed on 13 Dec 2013.

	Time (UTC)	Flight altitude (km)	Leg length (km)	Lidar mode	Horizontal resolution (km)
Leg 1	0648–0725	5.7	495.5	Fixed LOS	0.225
Leg 2	0731–0820	7.4	479.6	Scanning	7.74

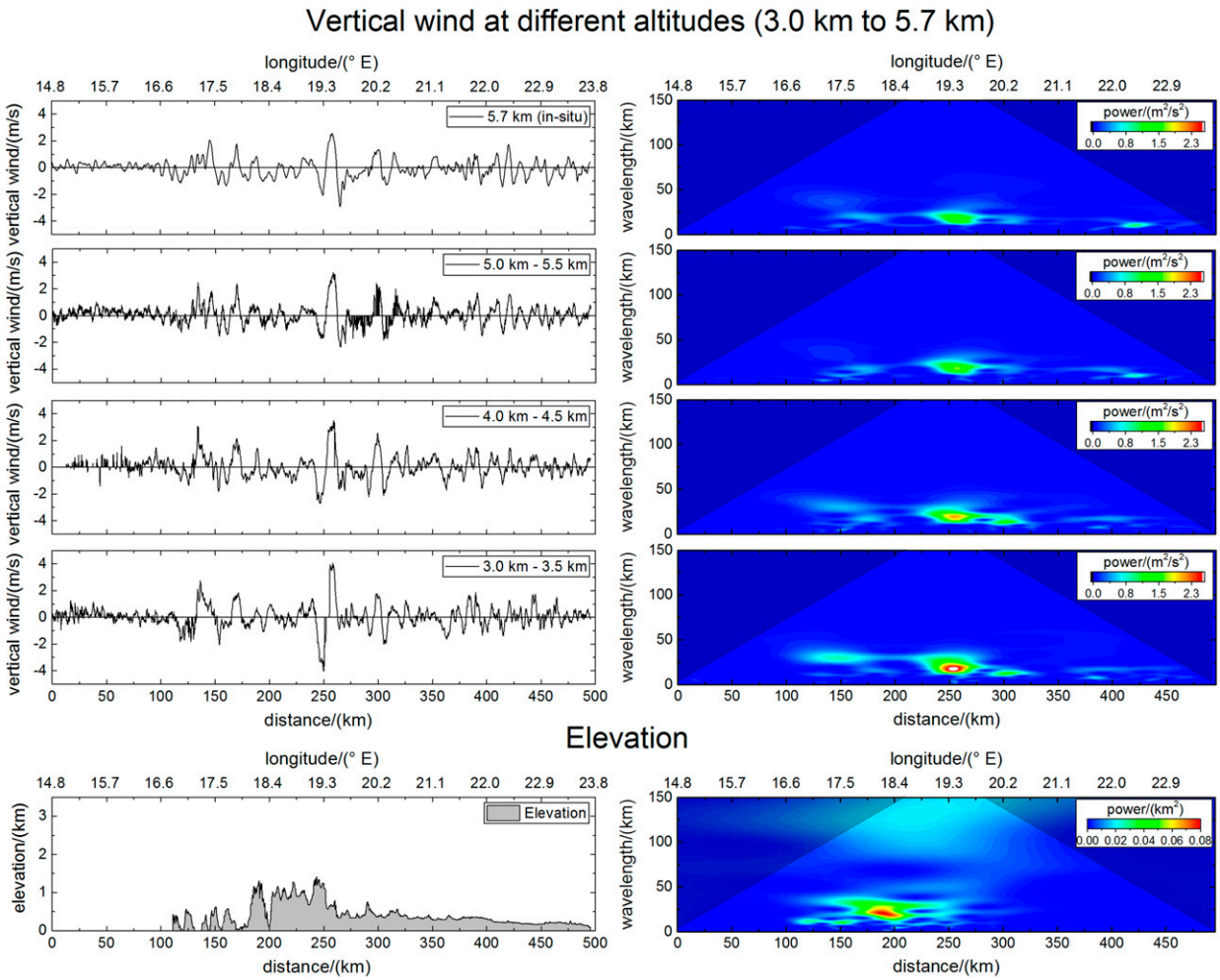

FIG. 9. (left) Vertically averaged vertical wind derived from DWL measurements at different altitudes (3.0–3.5, 4.0–4.5, 5.0–5.5 km) and vertical wind speed from in situ measurements at flight level. Orography is indicated in the lowermost panel. (right) Corresponding wavelet power spectra, calculated by using a Morlet wavelet (Torrence and Compo 1998).

b. *Horizontal wind measurements*

The horizontal wind speed and direction derived from lidar measurements (section 3c) acquired during the second flight leg are shown in Fig. 10 (top left and bottom left, respectively). The data measured by the nose-boom-mounted five-hole probe at flight level (7.4 km) are additionally indicated. The wind was constantly blowing from the northwesterly direction (≈315°) except for a directional wind shear measured between 0 and 3 km (≈21.0°−23.5°E; distance = 320 km − 480 km) in the eastern part of the flight leg. Besides the constant wind speed of about 20 m s^{-1} from the ground up to 6 km, a jet stream with wind speeds up to 45 m s^{-1} existed at the beginning of the flight leg, starting at around 6-km altitude. The in situ–measured wind speed confirmed the occurrence of the jet stream for higher altitudes.

To obtain information about the propagation behavior of the existing GWs, perturbations of $\mathbf{v}'_{\mathrm{hor}}$ are calculated (Fig. 10, right). To do so, a background wind profile needs to be estimated and subtracted from the measured wind speed. Based on Rayleigh lidar measurements, Ehard et al. (2015) discussed common background estimation methods—for instance, applying a running mean, a sliding polynomial fit method, or low-pass filtering—and their respective spectral influence on the retrieved perturbations. They find that a Butterworth filter performs best for analyzing GWs with a wide range of periods, whereas the running mean method gives good results only for shorter periods.

Different from Rayleigh lidars, where the background wind is determined in the vertical, the background wind has to be determined along the flight track for airborne DWL measurements. To do so, an ordinary fifth-order

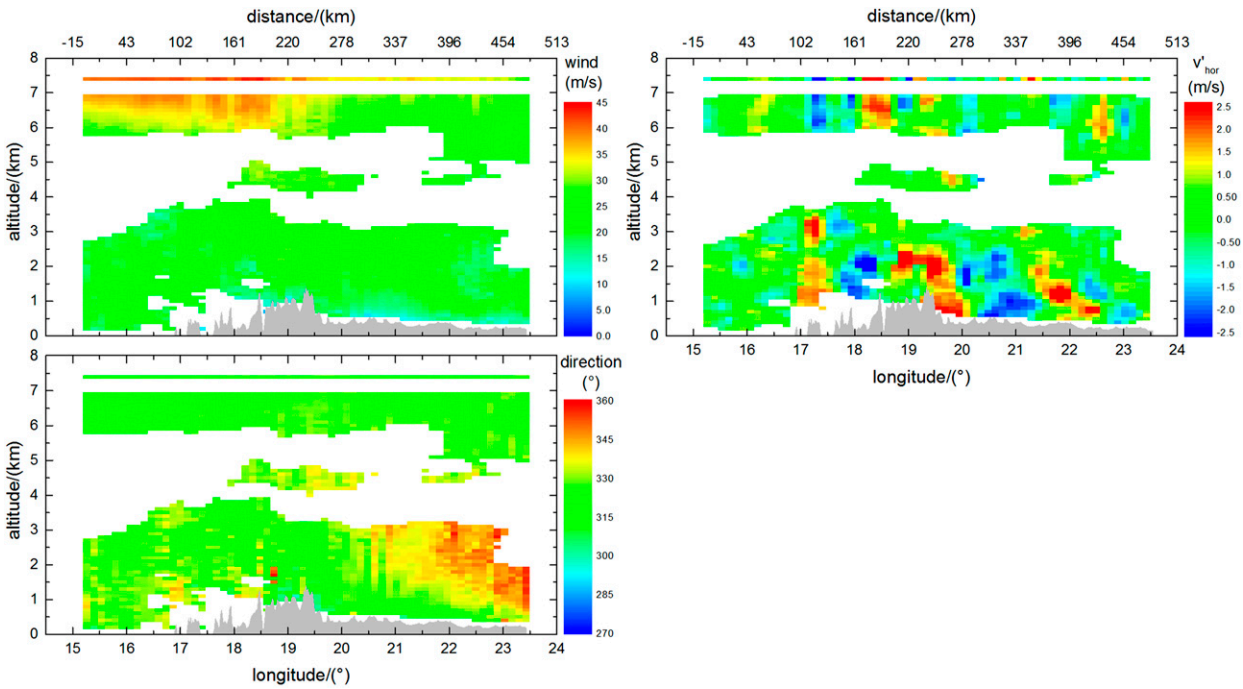

FIG. 10. (top left) Horizontal wind speed and (bottom left) wind direction derived from the lidar measurements during a cross-mountain leg flown 0731–0820 UTC 13 Dec 2013 (flight altitude = 7.4 km, leg length = 479.6 km, horizontal resolution = 7.74 km). Bars at 7.4-km altitude indicate the in situ wind data. Flight track is shown in Fig. 3 (red). (right) Corresponding $\mathbf{v}'_{\mathrm{hor}}$ derived from lidar measurements.

polynomial fit is applied in the horizontal direction per each range gate altitude and used as the background horizontal wind speed for subtraction (Fig. 10, right).

It can be seen that the amplitudes of $\mathbf{v}'_{\mathrm{hor}}$ reach values up to $\pm 2\,\mathrm{m\,s^{-1}}$. In the excitation region from the ground up to 3 km leeward, the highest elevation along the flight track (≈19.0°−23.5°E; distance = 220 km − 480 km), the wave fronts of the wind perturbations are tilted against the wind direction, as is expected for vertically propagating hydrostatic mountain waves (e.g., Nappo 2013, chapter 3). The largest tilt is occurring in the region between ≈21.5° and 23.0°E (distance = 367 km − 454 km). In the western part of the flight leg, and even more recognizable in the jet stream region, however, the wave fronts are vertically orientated. It is worth mentioning that the vertical orientation of the $\mathbf{v}'_{\mathrm{hor}}$ areas extends to altitudes of 7.4 km as seen from the in situ data. As shown by Bossert et al. (2015) based on airborne temperature lidar measurements during the DEEPWAVE campaign over New Zealand (Fritts et al. 2016), such small-scale waves can propagate up to the mesosphere and transport momentum up into that region.

Additionally, the horizontal wind speed perturbations at 1.8 and 6.7 km, and the elevation along the flight track (left) and the corresponding wavelet power spectra (right) are calculated as shown in Fig. 11. It can be seen that, different from the vertical wind spectra, $\mathbf{v}'_{\mathrm{hor}}$ spectra are extended along the entire flight leg. In the excitation region (1.8-km altitude), the dominating wavelengths lay between 100 and 125 km and an additional weaker feature is recognizable for wavelengths on the order of 25 km. At 6.7 km, the power spectrum looks more complex. The orographically excited waves in this region might be additionally influenced by the jet stream (Plougonven and Zhang 2014) and the tropopause (Whiteway et al. 2003), leading to a wave spectrum with wavelengths from 15 to 140 km. Comparing the $\mathbf{v}'_{\mathrm{hor}}$ spectrum in the excitation region (1.8 km) with the elevation spectrum (Fig. 11, bottom), it gets obvious that the horizontal wind speeds are mostly influenced by the long-wave part of the orography. Still, the short-wave part (10–40 km) is weakly represented. Compared to that, the vertical wind speed shows only spectral features of the short-wave part.

With the discussion given above, it is demonstrated that airborne horizontal wind lidar measurements are a valuable tool for GW characterization, especially in the excitation region but also for investigating the propagation behavior in the entire troposphere.

5. Summary and conclusions

Airborne coherent DWL measurements acquired on 13 December 2013 in the framework of the GW-LCYCLE I

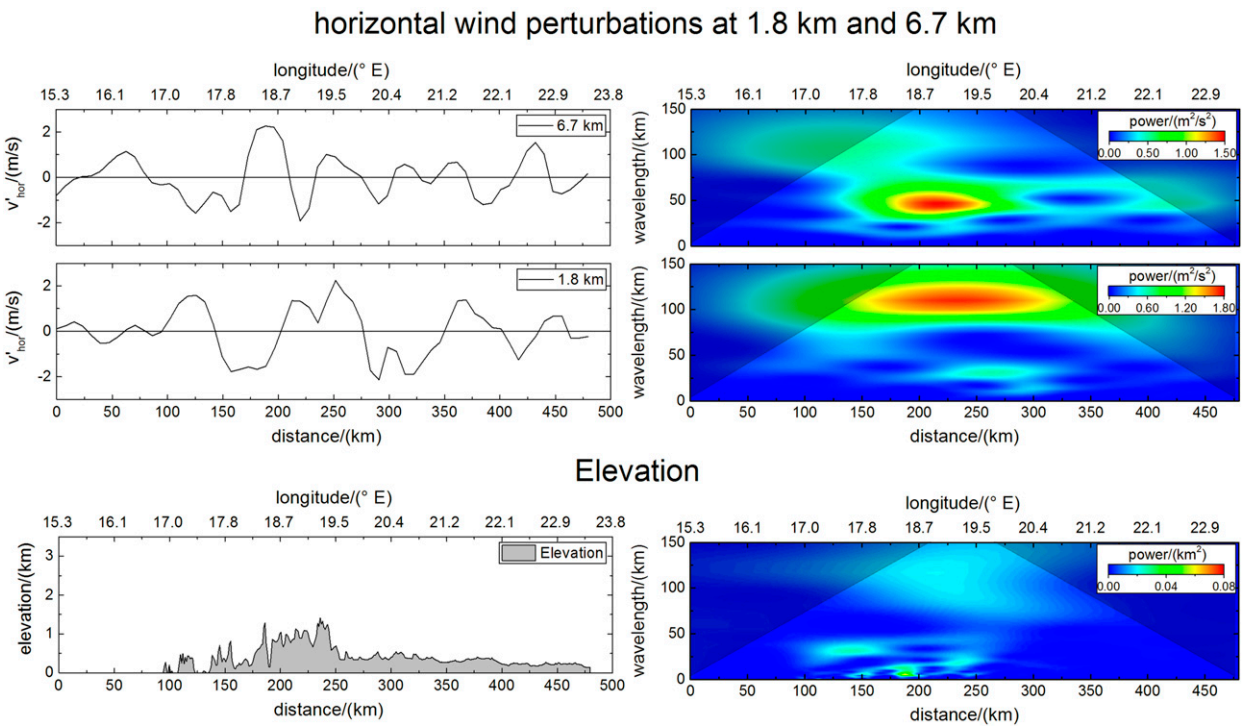

FIG. 11. (left) Horizontal wind perturbations measured at 1.8- and 6.7-km altitude. (bottom left) Graph indicates the orography. (right) Corresponding wavelet power spectra, calculated by using a Morlet wavelet (Torrence and Compo 1998).

campaign performed from 2 to 14 December 2013 in Kiruna, Sweden (67.8°N, 20.3°E), have been used to investigate internal gravity waves (GWs) induced by flow across the Scandinavian Mountains. The setup, the operation principle, and the corresponding data retrievals of the DLR's DWL were discussed, showing that vertical wind speed can be derived with a bias of less than $0.05\,\mathrm{m\,s^{-1}}$ and a standard deviation of $0.2\,\mathrm{m\,s^{-1}}$ with a horizontal resolution of 200 m and a vertical resolution of 100 m by correcting horizontal wind projections by means of ECMWF wind speed data. Furthermore, the horizontal wind vector was retrieved from lidar measurements by applying a velocity–azimuth display scan and a modified spectral accumulation technique, leading to reliable wind speed data with a horizontal resolution of 9 km and a vertical resolution of 100 m.

Both vertical and horizontal wind measurements are shown to be valuable for characterizing GW properties. Because of the high horizontal resolution of the DWL measurements, GW source spectra are analyzed for wavelengths down to 400 m for vertical wind measurement, and 18 km for horizontal wind speeds. The upper wavelength limit is defined by the maximum flight leg length to be about 250 km for 500-km-long flight legs.

Wavelet power spectra of the vertical wind measured in different altitudes demonstrate that the GW spectrum is dominated by wavelengths of 10–30 km and that the GW amplitude is decreasing with increasing altitude. Compared to that, the spectrum of the horizontal wind speed perturbations in the excitation region is dominated by wavelengths of 100–125 km.

It is shown that the spectrum of the topography is also composed of two distinct spectral regions: a short-wave region between 10 and 40 km, and a long-wave region between 80 and 150 km. Thus, it was concluded that the vertical wind speed spectrum is mostly dominated by the short-wave spectrum of the topography, whereas the spectrum of horizontal wind speed perturbations is dominated by the long-wave part but additionally shows an influence on the shorter wavelengths.

In the future, it is planned to adapt the scan pattern of the lidar measuring consecutively with a certain off-nadir angle with forward/backward pointing beams with respect to the flight direction. Such a procedure may enable measuring the horizontal wind speed in the flight direction and the vertical wind speed with a high horizontal resolution of a few hundred meters and thus giving the possibility of estimating the vertical flux of the horizontal momentum, which is proportional to $u'w'$, where u' and w' are the disturbances in the horizontal and vertical wind components, respectively.

Acknowledgments. We especially thank R. Simmet and E. Nagel for the technical support, C. Lemmerz and F. Chouza for the fruitful discussions, O. Reitebuch for the extensive internal review, and C. Mallaun from the DLR flight facility for providing Falcon in situ data. Further, we thank three anonymous reviewers for providing helpful comments about the manuscript. Part of this work was supported by the project "Investigation of the Life Cycle of Gravity Waves" (GW-LCYCLE) in the framework of the research initiative the Role of the Middle Atmosphere in Climate (ROMIC) funded by the German Federal Ministry of Education and Research under Grant 01LG1206A.

REFERENCES

Baumgarten, G., 2010: Doppler Rayleigh/Mie/Raman lidar for wind and temperature measurements in the middle atmosphere up to 80 km. *Atmos. Meas. Tech.*, **3**, 1509–1518, doi:10.5194/amt-3-1509-2010.

Beyon, J. Y., G. E. Arthur, G. J. Koch, and M. J. Kavaya, 2012: Noise whitening in airborne wind profiling with a pulsed 2-micron coherent Doppler lidar at NASA Langley Research Center. *Laser Radar Technology and Applications XVII*, M. D. Turner and G. W. Kamerman, Eds., International Society for Optics and Photonics (SPIE Proceedings, Vol. 8379), 83790N, doi:10.1117/12.919246.

Bluman, W., and J. E. Hart, 1988: Airborne Doppler lidar wind field measurements of waves in the lee of Mount Shasta. *J. Atmos. Sci.*, **45**, 1571–1583, doi:10.1175/1520-0469(1988)045<1571:ADLWFM>2.0.CO;2.

Bossert, K., and Coauthors, 2015: Momentum flux estimates accompanying multiscale gravity waves over Mount Cook, New Zealand, on 13 July 2014 during the DEEPWAVE campaign. *J. Geophys. Res. Atmos.*, **120**, 9323–9337, doi:10.1002/2015JD023197.

Browning, K., and R. Wexler, 1968: The determination of kinematic properties of a wind field using Doppler radar. *J. Appl. Meteor.*, **7**, 105–113, doi:10.1175/1520-0450(1968)007<0105:TDOKPO>2.0.CO;2.

Chen, C.-C., G. J. Hakim, and D. R. Durran, 2007: Transient mountain waves and their interaction with large scales. *J. Atmos. Sci.*, **64**, 2378–2400, doi:10.1175/JAS3972.1.

Chouza, F., O. Reitebuch, S. Groß, S. Rahm, V. Freudenthaler, C. Toledano, and B. Weinzierl, 2015: Retrieval of aerosol backscatter and extinction from airborne coherent Doppler wind lidar measurements. *Atmos. Meas. Tech.*, **8**, 2909–2926, doi:10.5194/amt-8-2909-2015.

——, ——, M. Jähn, S. Rahm, and B. Weinzierl, 2016: Vertical wind retrieved by airborne lidar and analysis of island induced gravity waves in combination with numerical models and in situ particle measurements. *Atmos. Chem. Phys.*, **16**, 4675–4692, doi:10.5194/acp-16-4675-2016.

Dörnbrack, A., M. Leutbecher, J. Reichardt, A. Behrendt, K.-P. Muller, and G. Baumgarten, 2001: Relevance of mountain wave cooling for the formation of polar stratospheric clouds over Scandinavia: Mesoscale dynamics and observations for January 1997. *J. Geophys. Res.*, **106**, 1569–1581, doi:10.1029/2000JD900194.

Duck, T. J., and J. A. Whiteway, 2005: The spectrum of waves and turbulence at the tropopause. *Geophys. Res. Lett.*, **32**, L07801, doi:10.1029/2004GL021189.

Ehard, B., B. Kaifler, N. Kaifler, and M. Rapp, 2015: Evaluation of methods for gravity wave extraction from middle-atmospheric lidar temperature measurements. *Atmos. Meas. Tech.*, **8**, 4645–4655, doi:10.5194/amt-8-4645-2015.

——, P. Achtert, A. Dörnbrack, S. Gisinger, J. Gumbel, M. Khaplanov, M. Rapp, and J. Wagner, 2016: Combination of lidar and model data for studying deep gravity wave propagation. *Mon. Wea. Rev.*, **144**, 77–98, doi:10.1175/MWR-D-14-00405.1.

Frehlich, R., 2001a: Errors for space-based Doppler lidar wind measurements: Definition, performance, and verification. *J. Atmos. Oceanic Technol.*, **18**, 1749–1772, doi:10.1175/1520-0426(2001)018<1749:EFSBDL>2.0.CO;2.

——, 2001b: Estimation of velocity error for Doppler lidar measurements. *J. Atmos. Oceanic Technol.*, **18**, 1628–1639, doi:10.1175/1520-0426(2001)018<1628:EOVEFD>2.0.CO;2.

——, S. M. Hannon, and S. W. Henderson, 1997: Coherent Doppler lidar measurements of winds in the weak signal regime. *Appl. Opt.*, **36**, 3491–3499, doi:10.1364/AO.36.003491.

Fritts, D. C., and M. J. Alexander, 2003: Gravity wave dynamics and effects in the middle atmosphere. *Rev. Geophys.*, **41**, 1003, doi:10.1029/2001RG000106.

——, and Coauthors, 2016: The Deep Propagating Gravity Wave Experiment (DEEPWAVE): An airborne and ground-based exploration of gravity wave propagation and effects from their sources throughout the lower and middle atmosphere. *Bull. Amer. Meteor. Soc.*, **97**, 425–453, doi:10.1175/bams-d-14-00269.1.

Hannon, S. M., and S. W. Henderson, 1995: Wind measurement applications of coherent lidar. *Rev. Laser Eng.*, **23**, 124–130, doi:10.2184/lsj.23.124.

Henderson, S. W., E. H. Yuen, and E. S. Fry, 1986: Fast resonance-detection technique for single-frequency operation of injection-seeded Nd:YAG lasers. *Opt. Lett.*, **11**, 715–717, doi:10.1364/OL.11.000715.

——, C. P. Hale, J. R. Magee, M. J. Kavaya, and A. V. Huffaker, 1991: Eye-safe coherent laser radar system at 2.1 μm using Tm, Ho:YAG lasers. *Opt. Lett.*, **16**, 773–775, doi:10.1364/OL.16.000773.

——, P. J. Suni, C. P. Hale, S. Hannon, J. R. Magee, D. L. Bruns, and E. H. Yuen, 1993: Coherent laser radar at 2 μm using solid-state lasers. *IEEE Trans. Geosci. Remote Sens.*, **31**, 4–15, doi:10.1109/36.210439.

Hildebrand, J., G. Baumgarten, J. Fiedler, U.-P. Hoppe, B. Kaifler, F.-J. Lübken, and B. Williams, 2012: Combined wind measurements by two different lidar instruments in the Arctic middle atmosphere. *Atmos. Meas. Tech.*, **5**, 2433–2445, doi:10.5194/amt-5-2433-2012.

Kaifler, B., N. Kaifler, B. Ehard, A. Dörnbrack, M. Rapp, and D. C. Fritts, 2015: Influences of source conditions on mountain wave penetration into the stratosphere and mesosphere. *Geophys. Res. Lett.*, **42**, 9488–9494, doi:10.1002/2015GL066465.

Kiemle, C., and Coauthors, 2007: Latent heat flux profiles from collocated airborne water vapor and wind lidars during IHOP_2002. *J. Atmos. Oceanic Technol.*, **24**, 627–639, doi:10.1175/JTECH1997.1.

Köpp, F., S. Rahm, and I. Smalikho, 2004: Characterization of aircraft wake vortices by 2-μm pulsed Doppler lidar. *J. Atmos. Oceanic Technol.*, **21**, 194–206, doi:10.1175/1520-0426(2004)021<0194:COAWVB>2.0.CO;2.

Nappo, C. J., 2013: *An Introduction to Atmospheric Gravity Waves.* 2nd ed. International Geophysics Series, Vol. 102, Academic Press, 359 pp.

O'Connor, E. J., A. J. Illingworth, I. M. Brooks, C. D. Westbrook, R. J. Hogan, F. Davies, and B. J. Brooks, 2010: A method for estimating the turbulent kinetic energy dissipation rate from a vertically pointing Doppler lidar, and independent evaluation from balloon-borne in situ measurements. *J. Atmos. Oceanic Technol.*, **27**, 1652–1664, doi:10.1175/2010JTECHA1455.1.

Plougonven, R., and F. Zhang, 2014: Internal gravity waves from atmospheric jets and fronts. *Rev. Geophys.*, **52**, 33–76, doi:10.1002/2012RG000419.

Reitebuch, O., 2012: Wind lidar for atmospheric research. *Atmospheric Physics: Background–Methods–Trends*, U. Schumann, Ed., Research Topics in Aerospace, Springer, 487–507, doi:10.1007/978-3-642-30183-4_30.

Smalikho, I., 2003: Techniques of wind vector estimation from data measured with a scanning coherent Doppler lidar. *J. Atmos. Oceanic Technol.*, **20**, 276–291, doi:10.1175/1520-0426(2003)020<0276:TOWVEF>2.0.CO;2.

Smith, R. B., 1989: Hydrostatic airflow over mountains. *Advances in Geophysics*, Vol. 31, Academic Press, 1–41, doi:10.1016/S0065-2687(08)60052-7.

——, B. K. Woods, J. Jensen, W. A. Cooper, J. D. Doyle, Q. Jiang, and V. Grubišić, 2008: Mountain waves entering the stratosphere. *J. Atmos. Sci.*, **65**, 2543–2562, doi:10.1175/2007JAS2598.1.

——, and Coauthors, 2016: Stratospheric gravity wave fluxes and scales during DEEPWAVE. *J. Atmos. Sci.*, **73**, 2851–2869, doi:10.1175/JAS-D-15-0324.1.

Teixeira, M. A. C., 2014: The physics of orographic gravity wave drag. *Front. Phys.*, **2**, 43, doi:10.3389/fphy.2014.00043.

Torrence, C., and G. P. Compo, 1998: A practical guide to wavelet analysis. *Bull. Amer. Meteor. Soc.*, **79**, 61–78, doi:10.1175/1520-0477(1998)079<0061:APGTWA>2.0.CO;2.

Vadas, S., J. Yue, and T. Nakamura, 2012: Mesospheric concentric gravity waves generated by multiple convective storms over the North American Great Plain. *J. Geophys. Res.*, **117**, D07113, doi:10.1029/2011JD017025.

Wagner, J., and Coauthors, 2017: Observed versus simulated mountain waves over Scandinavia—Improvement of vertical winds, energy and momentum fluxes by enhanced model resolution? *Atmos. Chem. Phys.*, **17**, 4031–4052, doi:10.5194/acp-17-4031-2017.

Weissmann, M., F. J. Braun, L. Gantner, G. J. Mayr, S. Rahm, and O. Reitebuch, 2005a: The Alpine mountain–plain circulation: Airborne Doppler lidar measurements and numerical simulations. *Mon. Wea. Rev.*, **133**, 3095–3109, doi:10.1175/MWR3012.1.

——, R. Busen, A. Dörnbrack, S. Rahm, and O. Reitebuch, 2005b: Targeted observations with an airborne wind lidar. *J. Atmos. Oceanic Technol.*, **22**, 1706–1719, doi:10.1175/JTECH1801.1.

Whiteway, J. A., E. G. Pavelin, R. Busen, J. Hacker, and S. Vosper, 2003: Airborne measurements of gravity wave breaking at the tropopause. *Geophys. Res. Lett.*, **30**, 2070, doi:10.1029/2003GL018207.

Witschas, B., S. Rahm, J. Wagner, and A. Dörnbrack, 2016: Airborne coherent Doppler Wind Lidar measurements of vertical and horizontal wind speeds for the investigation of gravity waves. *18th Coherent Laser Radar Conference (CLRC 2016)*, CIRES, 21–25.